Appl. Phys. B 77, 719–731 (2003)
DOI: 10.1007/s00340-003-1318-0

Applied Physics B
Lasers and Optics

H. MÜLLER[1,2,✉]
S. HERRMANN[1,2]
C. BRAXMAIER[3]
S. SCHILLER[4]
A. PETERS[1]

Precision test of the isotropy of light propagation

[1] Institut für Physik, Humboldt-Universität zu Berlin, Hausvogteiplatz 5–7, 10117 Berlin, Germany
[2] Fachbereich Physik, Universität Konstanz, 78457 Konstanz, Germany
[3] Astrium GmbH, An der B31, 88039 Friedrichshafen, Germany
[4] Institut für Experimentalphysik, Heinrich-Heine-Universität Düsseldorf, 40225 Düsseldorf, Germany

Received: 5 August 2003/Revised version: 10 September 2003
Published online: 4 November 2003 •

ABSTRACT We report on a test of the isotropy of light propagation performed by comparing the resonance frequencies of two orthogonal cryogenic optical resonators subject to Earth's rotation over ~ 1 yr. The technical aspects of the experiment are discussed and the analysis of the data is presented in detail. For a possible anisotropy of the speed of light c, we obtain $\Delta_\theta c/c_0 = (2.6 \pm 1.7) \times 10^{-15}$. Within the general extension of the standard model of particle physics, we extract limits on seven parameters at accuracies down to 10^{-15}, improving the best previous result by about two orders of magnitude. Within the Robertson–Mansouri–Sexl test theory, this implies an isotropy-violation parameter $\beta - \delta - \frac{1}{2} = (2.2 \pm 1.5) \times 10^{-9}$, about three times lower than the best previous result.

PACS 03.30.+p; 12.60.-i; 06.30.Ft

1 Introduction

Special relativity (SR) is a fundamental theory that describes how the concepts of space and time must be applied when describing physical phenomena in flat space–time. It therefore underlies all established theories of the forces of nature, from the gravitational and electromagnetic to the weak and strong nuclear forces. With the enormous advances in the technology of time, length, and frequency measurement, the effects of SR have become important even in daily measurement practice; for example, since 1983 the definition of the meter is based on the constancy of the velocity of light c, one of the foundations of SR. Positioning by means of the global positioning system, a technique that is quickly penetrating modern life, can only be applied if the (special and general) relativistic frequency shifts of the atomic clocks onboard the satellites are taken into account. Because of its importance, SR has been and must be tested with increasing precision in order to provide a firm basis for its future application, be it within fundamental science or within measurement technology. Indeed, tests of SR and general relativity (GR) have a long and fascinating history that spans the whole period of modern physics, starting with the famous Michelson–Morley (MM) test of the isotropy of light propagation [1] that even predated the creation of SR (see Fig. 1). Over time, some of the tests have been improved in accuracy more than a million-fold, due to the application of new technologies as they came into operation, most notably atomic clocks and lasers.

Tests of relativity are also gaining more and more importance within the huge and challenging project of creating and verifying a theory that unifies all forces of nature. Such tests could, in the best case, discover a violation of some fundamental law that so far (i.e. at the current level of experimental accuracy) has been found to hold. In the 'worst' case, they will provide more and more stringent experimental bounds on the range of theoretical models of unification that theorists may conceive. In fact, many currently discussed models for a unified theory do violate the principles of special and general relativity. In string theory, for example, spontaneous symmetry breaking could cause Lorentz violation [2]. In loop gravity, modified Maxwell equations have been derived that are not necessarily Lorentz covariant [3, 4]. The natural energy scale for these theories is the Planck scale, $E_\mathrm{p} \sim 10^{19}$ GeV. Direct experimentation at the Planck scale is, unfortunately, not feasible. It is, however, possible to search for residual effects with experiments operating at the attainable energies but featuring extremely high precision. This approach is also of great theor-

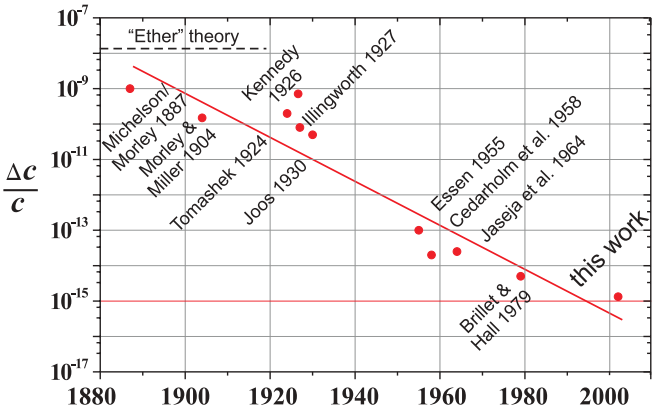

FIGURE 1 Accuracy of tests of the isotropy of electromagnetic wave propagation. $\Delta c = c(\theta) - c(\theta + \pi/2)$ is the established upper bound to the speed of light anisotropy. Experiments until 1930 were performed using optical interferometers, later experiments using electromagnetic cavities. The last three used lasers. The *line* is a guide for the eye

✉ Fax: +49-30/2093-4718,
E-mail: holger.mueller@physik.hu-berlin.de

etical interest: even if a definitive version of quantum gravity is not found in the near future, it is possible to state the most general low-energy limit and test this 'effective' theory. Such a theory has recently been formulated as a Lorentz-violating standard model extension (SME) [5–7], which has also suggested new tests to be performed. High-precision tests can bound parameters of this theory and thus restrict the parameter space of a future theory of quantum gravity. Considering the current dearth of experimental guidance, even a tiny experimental hint for or against models of quantum gravity would be of considerable value for the process of formulation of the theory.

Here, we present an experiment that tests the isotropy of the speed of c (Michelson–Morley experiment) and improves the classic 1979 result of Brillet and Hall [8] by a factor of three. Moreover, it explicitly determines a set of bounds on seven parameters of the Maxwell sector of the SME, with an accuracy about two orders of magnitude higher than the pioneering measurement [9]. Other parameters of this theory have been determined in astrophysical observations. These, however, cannot access all parameters of this theory, whereas laboratory experiments can [6]. The most important results of the experiment have been reported in a letter [10]. Here, we describe in detail the theoretical background, technology, data analysis, and interpretation of the experiment and its results.

The basic concept of the MM experiment described in this work is to measure the difference $\nu_x - \nu_y$ of the resonance frequencies ν_x and ν_y of two electromagnetic cavities pointing in orthogonal directions x and y in the laboratory frame as a function of the orientation and movement of the laboratory in space. The resonance frequencies of such a standing-wave Fabry–Pérot cavity are given by $\nu_{x,y} = m\, c_{x,y}/(2L)$, where $m \in \mathbb{N}$ is a constant mode number, L the cavity length, and $c_{x,y}$ the phase velocities of light (actually the averages of the velocities for forward and backward propagation) along the axes of the cavities. The measured deviations of the cavity frequency difference from a constant are analyzed in terms of a possible Lorentz-violating variation of c. In the framework of an assumed test theory (Sect. 2), bounds for parameters of the test theory can then be deduced. In practice, the frequency measurement is implemented by interrogating each cavity with a laser, and stabilizing ('locking') the laser frequency to the cavity (see Fig. 2). The frequencies of the lasers are then compared by measuring $\nu_x - \nu_y$.

The experimental method we employ relies on optical resonators cooled to temperatures near absolute zero, called cryogenic optical resonators (CORES). The resonators (see Fig. 3), fabricated from ultra-pure crystalline sapphire, exhibit a very low thermal expansion coefficient at cryogenic temperature. Moreover, they exhibit a remarkable absence of creep, i.e. they show no intrinsic length changes due to material relaxation. Together, these features imply that the length of a CORE has an outstanding constancy. They are therefore very well suited for tests of the constancy of the speed of light of the optical wave inside the cavity, which are performed over long times.

We also note that experiments using electromagnetic cavities, especially cryogenic resonators, are now employed by other groups in ongoing and future high-precision tests of relativity. For example, Wolf et al. [11] reported a new

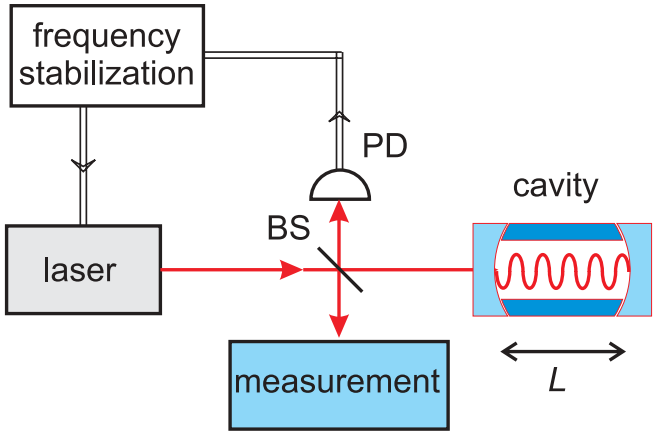

FIGURE 2 Interrogation of the cavity resonance frequency. A laser is coupled to the cavity and its frequency is locked to the resonance by a servo. The laser frequency is then measured. BS denotes a beam splitter, PD a photodetector

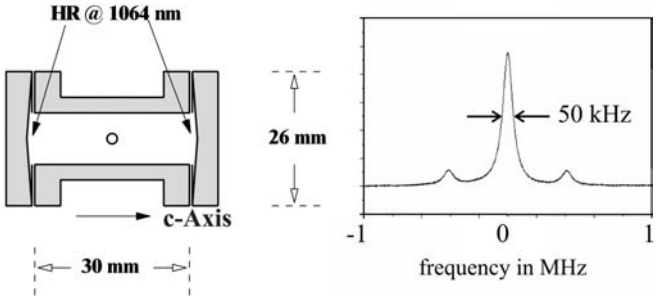

FIGURE 3 Schematic of a CORE as used in this experiment

Kennedy–Thorndike experiment (Sect. 2.2) using a cryogenic microwave resonator, which improves the limit previously set by our own test [12, 13]. A Michelson–Morley type of experiment using superconducting niobium microwave cavities, which was the first to report limits on the SME parameters as described above, was recently reported by Lipa et al. [9]. Space tests, to achieve the ultimate in performance in such experiments, with cavities on the International Space Station (SUMO [14]) and on a dedicated satellite (OPTIS [15]), are also being developed.

2 Theoretical framework

2.1 *Standard model extension*

Here we describe the SME and derive the hypothetical signal to be searched for in the experiment. The description of the SME is taken from [6] to introduce essential definitions required for the derivation.

The SME starts from a Lagrangian formulation of the standard model, adding all possible observer Lorentz scalars that can be formed from the known particles and Lorentz tensors. In the photonic sector, the Lagrangian is

$$\mathcal{L} = -\frac{1}{4}F^{\mu\nu}F_{\mu\nu} + \frac{1}{2}(k_{AF})^{\kappa}\varepsilon_{\kappa\lambda\mu\nu}A^{\lambda}F^{\mu\nu} - \frac{1}{4}(k_F)_{\kappa\lambda\mu\nu}F^{\kappa\lambda}F^{\mu\nu}\,, \tag{1}$$

where $F^{\mu\nu}$ is the electromagnetic field tensor and A^{μ} the vector potential. The first term is the usual Maxwell Lagrangian;

the other terms are Lorentz violating. The second term is expected to vanish for theoretical reasons and is constrained experimentally by cosmological birefringence measurements to levels well below those relevant here [16], so we can neglect it in what follows. The third term is proportional to a dimensionless tensor $(k_F)_{\kappa\lambda\mu\nu}$ that has the symmetries of the Riemann tensor plus a vanishing double trace. Thus, it contains 19 independent components.

The inhomogeneous Maxwell equations in vacuum following from this Lagrangian, namely

$$\partial_\alpha F^\alpha_\mu + (k_F)_{\mu\alpha\beta\gamma}\partial^\alpha F^{\beta\gamma} = 0\,, \tag{2}$$

and the homogenous equations

$$\partial_\mu \tilde{F}^{\mu\nu} = 0 \tag{3}$$

can be written in analogy to the Maxwell equations in anisotropic media: with the 3×3 matrices

$$(\kappa_{DE})^{jk} = -2(k_F)^{0j0k}\,, \tag{4}$$

$$(\kappa_{HB})^{jk} = \frac{1}{2}\epsilon^{jpq}\epsilon^{krs}(k_F)^{pqrs}, \tag{5}$$

$$(\kappa_{DB})^{jk} = (k_F)^{0jpq}\epsilon^{kpq}\,, \tag{6}$$

$$(\kappa_{HE})^{kj} = -(\kappa_{DB})^{jk} \tag{7}$$

one can define $\boldsymbol{D}$ and $\boldsymbol{H}$ fields

$$\begin{pmatrix}\boldsymbol{D}\\ \boldsymbol{H}\end{pmatrix} = \begin{pmatrix}\mathbf{1}+\kappa_{DE} & \kappa_{DB}\\ \kappa_{HE} & \mathbf{1}+\kappa_{HB}\end{pmatrix}\begin{pmatrix}\boldsymbol{E}\\ \boldsymbol{B}\end{pmatrix}\,, \tag{8}$$

where $\mathbf{1}$ represents the 3×3 unit matrix. The Maxwell equations can now be expressed as

$$\boldsymbol{\nabla}\times\boldsymbol{H} - \partial_0\boldsymbol{D} = 0\,, \tag{9}$$

$$\boldsymbol{\nabla}\times\boldsymbol{E} + \partial_0\boldsymbol{B} = 0\,, \tag{10}$$

$$\boldsymbol{\nabla}\cdot\boldsymbol{D} = 0\,, \tag{11}$$

$$\boldsymbol{\nabla}\cdot\boldsymbol{B} = 0\,. \tag{12}$$

Lorentz violation in electrodynamics thus corresponds to electrodynamics in anisotropic media. It is convenient to introduce the linear combinations

$$(\tilde{\kappa}_{e+})^{jk} = \frac{1}{2}(\kappa_{DE}+\kappa_{HB})^{jk}\,, \tag{13}$$

$$(\tilde{\kappa}_{o+})^{jk} = \frac{1}{2}(\kappa_{DB}+\kappa_{HE})^{jk}\,, \tag{14}$$

$$(\tilde{\kappa}_{e-})^{jk} = \frac{1}{2}(\kappa_{DE}-\kappa_{HB})^{jk} - \frac{1}{3}\delta^{jk}(\kappa_{DE})^{ll}\,, \tag{15}$$

$$(\tilde{\kappa}_{o-})^{jk} = \frac{1}{2}(\kappa_{DB}-\kappa_{HE})^{jk}\,, \tag{16}$$

$$\tilde{\kappa}_{tr} = \frac{1}{3}(\kappa_{DE})^{ll}\,. \tag{17}$$

Two of these, $(\tilde{\kappa}_{e+})^{jk}$ and $(\tilde{\kappa}_{o-})^{jk}$, control the dependence of the propagation of light on its polarization and have been restricted by studying light from astronomical sources to $< 2\times 10^{-32}$ [6], so we can assume $(\tilde{\kappa}_{e+})^{jk} = (\tilde{\kappa}_{o-})^{jk} = 0$ in the following. This restricts 10 of the 19 degrees of freedom of $(k_F)_{\kappa\lambda\mu\nu}$. The further terms lead to a change δc of the phase velocity of light, which can be measured in cavity experiments like the one presented here.

The principle of such a measurement is studying the rotation invariance of the resonance frequency $\nu_{\rm cav}$ of an electromagnetic cavity, which is proportional to the velocity of light along the cavity axis. Thus, a Lorentz-violating shift $\delta c/c$ of the velocity of light leads to an equal relative shift $\delta\nu_{\rm cav}/\nu_{\rm cav}$ (assuming a constant cavity length L, see below) independent of the polarization. It can be expressed within the SME as [6]

$$\frac{\delta\nu_{\rm cav}}{\nu_{\rm cav}} = \frac{1}{2}[(\hat{N}\times\hat{E}^*)(\kappa_{HB})_{\rm lab}(\hat{N}\times\hat{E}) - \hat{E}^*(\kappa_{DE})_{\rm lab}\hat{E}]\,. \tag{18}$$

Here, $\hat{N}$ denotes a unit vector that specifies the cavity orientation and $\hat{E}$ a unit vector normal to $\hat{N}$ that specifies the polarization. The cavity frequency shift given by this expression is independent of the polarization if $\kappa_{DE} = -\kappa_{HB}$ is inserted, which follows from $(\tilde{\kappa}_{e+})^{jk} = 0$. The notation $(\kappa_{HB})_{\rm lab}$, $(\kappa_{DE})_{\rm lab}$ indicates that the matrices are given in the laboratory frame of the cavity.

The dependence of the cavity length on the elements of $(k_F)_{\kappa\lambda\mu\nu}$ has been investigated in [17]: the Lorentz-violating electrodynamics necessarily leads to a modification of the Coulomb interaction given by κ_{DE}. Since the geometry of crystals is largely determined by Coulomb interactions, a change of the cavity length connected to κ_{DE} will arise and modify the sensitivity of the relative frequency shift $\delta\nu_{\rm cav}/\nu_{\rm cav} = \delta c/c - \delta L/L$ to Lorentz violation. For ionic materials, an increase of the sensitivity by material-dependent factors around 2 has been found [17]. For the material used for our CORE*s*, sapphire (that has strong covalent bonds), the estimated increase is only a few percent [17]. We can therefore neglect the length change and proceed using (18).

2.1.1 Derivation of the signal in the laboratory frame. We use two frames of reference, in accordance with [6]: a Sun-centered standard frame (4-vector components in this frame are denoted by Greek indices, spatial components by capital Latin indices), and a laboratory frame (spatial components in the laboratory frame are denoted by small Latin indices a, b, c, ...).

The Sun-centered frame is suitable as a standard frame for expressing values of $(k_F)_{\kappa\lambda\mu\nu}$ because it is inertial over all time scales relevant for the experiment. It has the X axis pointing towards the vernal equinox (spring point) at 0 h right ascension and 0° declination, the Z axis pointing towards the celestial north pole (90° declination), and the Y axis in the way needed to complete the right-handed orthogonal dreibein. Earth's equatorial plane lies within the X–Y plane and the orbital plane of the Earth is tilted at an angle $\eta \simeq 23°$ with respect to the latter. The time scale T is set by $T = 0$ when the Sun passes the spring point, which in 2001 happened on March 20, 13 h 31 min Universal Time (UT).

The laboratory frame has the x axis pointing south, the y axis east, and the z axis vertically upwards. The laboratory time scale is set by $T_\oplus = 0$ at the instant when the y and the Y axes coincide, e.g. on March 20, 2001, 11:31 UT for our experiment, when in Konstanz the Sun passes the zenith. Then the direction of the radius of the Earth, drawn from the Earth's

center to Konstanz and projected onto the equatorial plane, is parallel to the X axis, so that the y and the Y axes coincide.

To obtain the time dependence of the frequency of a cavity located on Earth from (18), the laboratory-frame matrices $(\kappa_{DE})_{\rm lab}$ and $(\kappa_{HB})_{\rm lab}$ can be obtained from the corresponding matrices in the Sun-centered standard frame using the transformations described in [6]. They involve Lorentz transformations according to the velocity $\beta_\oplus \sim 10^{-4}$ of Earth's orbit and the rotations from the Sun-centered frame to the laboratory defined by the rotation matrix

$$R = \begin{pmatrix} \cos\chi\cos\omega_\oplus T_\oplus & \cos\chi\sin\omega_\oplus T_\oplus & -\sin\chi \\ -\sin\omega_\oplus T_\oplus & \cos\omega_\oplus T_\oplus & 0 \\ \sin\chi\cos\omega_\oplus T_\oplus & \sin\chi\sin\omega_\oplus T_\oplus & \cos\chi \end{pmatrix}, \quad (19)$$

where $\chi \simeq 42.3^\circ$ is the colatitude of Konstanz. The resulting time dependency of $\delta\nu/\nu$ is given by the angular frequencies $\omega_\oplus \simeq 2\pi/(23\,\mathrm{h}\,56\,\mathrm{min})$ of Earth's rotation and $\Omega_\oplus = 2\pi/1\,\mathrm{yr}$. Due to the movement of the laboratory frame with $\beta_\oplus$ and a velocity $0 \le \beta_{\rm L} \le 1.5\times10^{-6}$ (dependent on the geographical latitude) due to Earth's rotation, some components of $(k_F)_{\kappa\lambda\mu\nu}$ enter the signal $\delta\nu/\nu$ directly, and some suppressed by $\beta_\oplus$ and/or $\beta_{\rm L}$.

The resulting frequency change of a single cavity can be expressed as [6]

$$\frac{\delta\nu}{\nu} = A' + B'\sin 2\theta + C\cos 2\theta\,, \quad (20)$$

where θ is the angle between the cavity axis and the north–south axis. A', B', and C are combinations of components of $(k_F)_{\kappa\lambda\mu\nu}$ defined in [6]. (The primes are introduced to prevent confusion with A and B introduced later in (24).) For our experiment, we measure the frequency difference $\nu_x - \nu_y$ of a cavity oriented north–south and a cavity oriented east–west, so $\theta_x = 0$ and $\theta_y = 90^\circ$. Therefore,

$$\frac{\delta(\nu_x - \nu_y)}{\nu} = 2C\,, \quad (21)$$

where $\nu \simeq \nu_x \simeq \nu_y$ is the average frequency. According to [6],

$$C = C_0 + C_1\sin\omega_\oplus T_\oplus + C_2\cos\omega_\oplus T_\oplus + C_3\sin 2\omega_\oplus T_\oplus + C_4\cos 2\omega_\oplus T_\oplus\,. \quad (22)$$

The coefficients C_0, ..., C_4 are given in Appendix E of [6]. We can simplify them by inserting $\tilde\kappa_{e+} = \tilde\kappa_{o-} = 0$, the result of the astrophysical polarization measurements [5, 6]. C_0, ..., C_4 are themselves time dependent, involving terms proportional to $\sin\Omega_\oplus T$ and $\cos\Omega_\oplus T$. For our experiment the difference of the time scales is $\delta T = T - T_\oplus \simeq 2\,\mathrm{h}$. Substituting $T = T_\oplus + \delta T$ into the sine and cosine functions and using trigonometric relations, one obtains additional terms that are proportional to $\sin\Omega_\oplus\delta T \simeq 2\times10^{-3}$. We now substitute C_0, ..., C_4 into (22). The resulting signal can be written as a Fourier series with signal components at six different frequencies $\omega_1 = \omega_\oplus$, $\omega_1^\pm = \omega_\oplus \pm \Omega_\oplus$, $\omega_2 = 2\omega_\oplus$, and $\omega_2^\pm = \omega_\oplus \pm \Omega_\oplus$:

$$\begin{aligned}\frac{\delta\nu}{\nu} = {} & c_S + s_1^-\sin\omega_1^- T_\oplus + c_1^-\cos\omega_1^- T_\oplus + s_1\sin\omega_1 T_\oplus \\ & + c_1\cos\omega_1 T_\oplus + s_1^+\sin\omega_1^+ T_\oplus + c_1^+\cos\omega_1^+ T_\oplus \\ & + s_2^-\sin\omega_2^- T_\oplus + c_2^-\sin\omega_2^- T_\oplus + s_2\sin\omega_2 T_\oplus \\ & + c_2\cos\omega_2 T_\oplus + s_2^+\sin\omega_2^+ T_\oplus + c_2^+\cos\omega_2^+ T_\oplus\,. \end{aligned} \quad (23)$$

The term c_S includes constants and terms that vary solely with the frequency $\Omega_\oplus$. The remaining signal amplitudes are

$$\begin{aligned} s_1^- &= \frac{\beta_\oplus}{2}\sin\chi\cos\chi[(\cos\eta+1)(\tilde\kappa_{o+})^{XY} - \cos\eta(\tilde\kappa_{o+})^{XZ}]\,, \\ c_1^- &= \frac{\beta_\oplus}{2}\sin\chi\cos\chi\sin\eta(\tilde\kappa_{o+})^{YZ}\,, \\ s_1 &= -\sin\chi\cos\chi(\tilde\kappa_{e-})^{YZ}\,, \\ c_1 &= -\sin\chi\cos\chi(\tilde\kappa_{e-})^{XZ}\,, \\ s_1^+ &= \frac{\beta_\oplus}{2}\sin\chi\cos\chi[(\cos\eta-1)(\tilde\kappa_{o+})^{XY} - \sin\eta(\tilde\kappa_{o+})^{XZ}]\,, \\ c_1^+ &= \frac{\beta_\oplus}{2}\sin\chi\cos\chi\sin\eta(\tilde\kappa_{o+})^{YZ}\,, \\ s_2^- &= -\frac{\beta_\oplus}{4}(1+\cos^2\chi)(\cos\eta+1)(\tilde\kappa_{o+})^{YZ}\,, \\ c_2^- &= -\frac{\beta_\oplus}{4}(1+\cos^2\chi)(1+\cos\eta)(\tilde\kappa_{o+})^{XZ}\,, \\ s_2 &= \frac{1}{2}(1+\cos^2\chi)(\tilde\kappa_{e-})^{XY}\,, \\ c_2 &= \frac{1}{4}(1+\cos^2\chi)[(\tilde\kappa_{e-})^{XX} - (\tilde\kappa_{e-})^{YY}]\,, \\ s_2^+ &= \frac{\beta_\oplus}{4}(1+\cos^2\chi)(1\text{-}\cos\eta)(\tilde\kappa_{o+})^{YZ}\,, \\ c_2^+ &= \frac{\beta_\oplus}{4}(1+\cos^2\chi)(1-\cos\eta)(\tilde\kappa_{o+})^{XZ}\,. \end{aligned}$$

It can be seen that the components of $\tilde\kappa_{o+}$ enter the experiment due to the movement of the laboratory with $\beta_\oplus$. Each coefficient might include terms suppressed by either $\beta_\oplus$, $\beta_{\rm L}$, or $\sin\Omega_\oplus\delta T$. These are only included if no term of larger order is present in the same coefficient. In effect, this removes all terms of orders $\beta_{\rm L}$ and $\sin\Omega_\oplus\delta T$. The fit accuracy in the experiments does not allow us to resolve a suppressed term that occurs at the same frequency as an unsuppressed term.

From the nine components of $(k_F)_{\kappa\lambda\mu\nu}$ that are not measured in astrophysical experiments, the parameter κ_{tr} (17) does not lead to any time-dependent signals to first order in $\beta_\oplus$ and $\beta_{\rm L}$ in any cavity experiment. On Earth, the parameter $(\tilde\kappa_{e-})^{ZZ}$ is measurable only by using a turntable, because the rotation axis of the laboratory frame, i.e. Earth's axis, coincides with the Z direction of the Sun-centered celestial equatorial reference frame adopted. The other seven independent parameter combinations can, however, be measured in our experiment.

2.2 *Kinematic framework for SR tests*

The Robertson–Mansouri–Sexl (RMS) framework [18] (see also [19] for a recent review) is a test theory of SR. According to this framework, SR follows from three experimental principles: the isotropy of the speed of light (MM test), the independence of the speed of light from the velocity of the laboratory (Kennedy–Thorndike test), and time dilation. The last has been tested by laser spectroscopic measurement of the Doppler shift of relativistic atoms [20, 21], and will not be considered further here. MM tests currently offer the highest precision and are thus the most sensitive probe for possible violations of SR.

The framework offers a useful way of parameterizing violations of Lorentz invariance. A preferred frame Σ, usu-

ally identified with the cosmic microwave background, is assumed, in which the speed of light c_0 is constant. The Lorentz transformations between Σ and a frame S moving with the velocity $\boldsymbol{v}$ with respect to Σ are replaced by generalized linear transformations. These depend solely on $\boldsymbol{v}$ and three phenomenological parameters, which reduce to special values if SR holds. In the moving frame S, the speed of light can be expressed to lowest order in v/c_0 as

$$\frac{c(\theta, v)}{c_0} = 1 + A\frac{v^2}{c_0^2} + B\frac{v^2}{c_0^2}\sin^2\theta\,. \tag{24}$$

(In the notation of [18] $A = -(\alpha - \beta + 1)$ and $B = -(\beta - \delta - 1/2)$.) The dimensionless parameters A and B vanish if special relativity is valid; otherwise the speed of light may depend on v and the angle θ between the direction of light propagation and $\boldsymbol{v}$. Kennedy–Thorndike experiments test $A = 0$ (also called boost invariance), MM experiments test $B = 0$ (rotation invariance). $A = 1$ and $B = -1/2$ would be the predictions of the pre-relativistic ether theory.

2.2.1 Derivation of the signal for the Robertson–Mansouri–Sexl test theory.

This experiment. For this calculation, we may neglect Earth's orbital velocity, as its inclusion would only lead to minor corrections to the hypothetical signal amplitudes as well as small signal components at additional frequencies, but would not enable us to measure additional parameters. The velocity vector $\boldsymbol{v}_{\rm cmb}$ of the motion of the Sun relative to the cosmic microwave background is given by the right ascension $\alpha = 168°$ (or 11.2 h) and $\beta = -6°$ declination at a speed of $v_{\rm cmb} = 369\,{\rm km/s}$ [22]. In the Sun-centered frame as described in Sect. 2.1.1

$$\boldsymbol{v}_{\rm cmb} = v_{\rm cmb}\,(-\cos\alpha\cos\beta,\ -\cos\beta\sin\alpha,\ -\sin\beta)\ . \tag{25}$$

Our cavities are parallel to the x and the y axes in the laboratory frame, respectively. Thus, the cavity orientations are given by the unit vectors $(\boldsymbol{e}_x)_{\rm lab} = (1, 0, 0)$ and $(\boldsymbol{e}_y)_{\rm lab} = (0, 1, 0)$. The rotations between the laboratory and the Sun-centered frames are given by the rotation matrix R (19). The unit vectors describing the cavity orientations in the Sun-centered frame:

$$\boldsymbol{e}_x = (\cos\chi\cos\omega_\oplus T_\oplus,\ \cos\chi\sin\omega_\oplus T_\oplus,\ -\sin\chi)\,, \tag{26}$$

$$\boldsymbol{e}_y = (-\sin\omega_\oplus T_\oplus,\ \cos\omega_\oplus T_\oplus,\ 0)\,. \tag{27}$$

are thus obtained.

In our experiment, the difference of the frequencies

$$\frac{\Delta\nu_x}{\nu_0} - \frac{\Delta\nu_y}{\nu_0} = B\frac{v^2}{c_0^2}\left(\sin^2\theta_x - \sin^2\theta_y\right) \tag{28}$$

of the two cavities oriented south and east is measured, where $\theta_{x,y}$ are the angles of the cavity axes with respect to the direction of $\boldsymbol{v}_{\rm cmb}$. $\theta_{1,2}$ are obtained within the Sun-centered frame by using

$$\sin^2\theta_{x,y} = 1 - \cos^2\theta_i = 1 - \frac{(\boldsymbol{v}_{\rm cmb}\boldsymbol{e}_{x,y})^2}{|v_{\rm cmb}|^2}\,. \tag{29}$$

We find

$$\begin{aligned}\sin^2\theta_x = 1 - [&-\cos\alpha\cos\beta\cos\chi\cos\omega_\oplus T_\oplus \\ &+ \sin\beta\sin\chi - \cos\beta\cos\chi\sin\alpha\sin\omega_\oplus T_\oplus]^2\,,\\ \sin^2\theta_y = 1 - [&-\cos\beta\cos\omega_\oplus T_\oplus\sin\alpha \\ &+ \cos\beta\cos\alpha\sin\omega_\oplus T_\oplus]^2\,.\end{aligned}$$

Using these expressions and simple trigonometric relations, we end up with

$$\begin{aligned}\frac{\Delta\nu}{\nu_0} = \frac{v^2}{c_0^2}(&\gamma_1\cos\omega_\oplus T_\oplus + \gamma_2\cos 2\omega_\oplus T_\oplus \\ &+ \sigma_1\sin\omega_\oplus T_\oplus + \sigma_2\sin 2\omega_\oplus T_\oplus)\,,\end{aligned} \tag{30}$$

where

$$\gamma_1 = 2\cos\alpha\cos\beta\sin\beta\cos\chi\sin\chi\,, \tag{31}$$

$$\gamma_2 = -\frac{1}{2}\cos 2\alpha\cos^2\beta(1+\cos^2\chi)\,, \tag{32}$$

$$\sigma_1 = 2\sin\alpha\cos\beta\sin\beta\cos\chi\sin\chi\,, \tag{33}$$

$$\sigma_2 = -\frac{1}{2}\sin 2\alpha\cos^2\beta(1+\cos^2\chi)\,. \tag{34}$$

The total signal amplitudes at $\omega_\oplus$ and $2\omega_\oplus$ are

$$\sqrt{\sigma_1^2+\gamma_1^2} = 2\cos\beta\sin\beta\cos\chi\sin\chi \simeq 0.10\,, \tag{35}$$

$$\sqrt{\sigma_2^2+\gamma_2^2} = \frac{1}{2}\cos^2\beta(1+\cos^2\chi) \simeq 0.77\,. \tag{36}$$

The experiment of Brillet and Hall. For comparison, we also calculate the signal components for the experiment of Brillet and Hall. Here, the frequency of a cavity rotating around the vertical axis has been compared to the frequency of a (non-rotating) methane frequency standard.

Assuming counterclockwise rotation with an angular frequency $\omega_{\rm r}$, the cavity orientation in the laboratory frame is described by the unit vector

$$(\boldsymbol{e}_{BH})_{\rm lab} = (\cos[\omega_r T_\oplus + \phi_0],\ -\sin[\omega_r T_\oplus + \phi_0],\ 0)\ , \tag{37}$$

where the angle ϕ_0 is between the orientation of the cavity at $T_\oplus = 0$ and the laboratory x axis. Rotating this into the Sun-centered frame and proceeding as above gives an expression for $\delta\nu/\nu$ containing oscillatory terms at many different frequencies that are summarized in Table 1.

Brillet and Hall reported the signal amplitudes that are the root of the sum of the squares of the sine and cosine components. These are given in Table 2.

2.3 *Cavity orientation in the laboratory for optimum sensitivity*

For technical reasons, both cavity axes should be horizontally oriented to minimize the gravitational influence on the cavities. Additionally, to provide maximum sensitivity, the two cavity axes should be normal to each other. The orientation of the cavities is chosen such that one cavity points north, the other east. On the one hand, this simplified fitting the experiment into our laboratory; on the other hand, it

Signal component	Amplitude/(Bv^2/c_0^2)
$\cos\omega_\oplus T_\oplus$	$\frac{1}{4}\cos\alpha\sin 2\beta\sin 2\chi$
$\cos 2\omega_\oplus T_\oplus$	$\frac{1}{4}\cos 2\alpha\cos^2\beta\sin^2\chi$
$\cos(2\omega_r T_\oplus+2\phi_0)$	$\frac{1}{8}(-1+3\cos 2\beta)\sin^2\chi$
$\cos[(2\omega_r+\omega_\oplus)T_\oplus+2\phi_0]$	$\frac{1}{2}\cos\alpha\cos\beta\sin\beta(1+\cos\chi)\sin\chi$
$\cos[2(\omega_r+\omega_\oplus)T_\oplus+2\phi_0]$	$\frac{1}{8}\cos 2\alpha\cos^2\beta(1+\cos\chi)^2$
$\cos[(2\omega_r-\omega_\oplus)T_\oplus+2\phi_0]$	$\frac{1}{2}\cos\alpha\cos\beta\sin\beta(\cos\chi-1)\sin\chi$
$\cos[2(\omega_r-\omega_\oplus)T_\oplus+2\phi_0]$	$\frac{1}{8}\cos 2\alpha\cos^2\beta(1-\cos\chi)^2)$
$\sin\omega_\oplus T_\oplus$	$-\frac{1}{4}\sin\alpha\sin 2\beta\sin 2\chi$
$\sin 2\omega_\oplus T_\oplus$	$-\frac{1}{4}\sin 2\alpha\cos^2\beta\sin^2\chi$
$\sin(2\omega_r T_\oplus+2\phi_0)$	0
$\sin[(2\omega_r+\omega_\oplus)T_\oplus+2\phi_0]$	$-\frac{1}{2}\sin\alpha\cos\beta\sin\beta(1+\cos\chi)\sin\chi$
$\sin[2(\omega_r+\omega_\oplus)T_\oplus+2\phi_0]$	$-\frac{1}{8}\sin 2\alpha\cos^2\beta(1+\cos\chi)^2$
$\sin[(2\omega_r-\omega_\oplus)T_\oplus+2\phi_0]$	$\frac{1}{2}\sin\alpha\cos\beta\sin\beta(\cos\chi-1)\sin\chi$
$\sin[2(\omega_r-\omega_\oplus)T_\oplus+2\phi_0]$	$\frac{1}{8}\sin 2\alpha\cos^2\beta(1-\cos\chi)^2$

TABLE 1 Sine and cosine signal components (divided by Bv^2/c_0^2) for the experiment of Brillet and Hall in the RMS test theory

Frequency	Amplitude/(Bv^2/c_0^2)
$\omega_\oplus$	$\frac{1}{4}\sin 2\beta\sin 2\chi$
$2\omega_\oplus$	$\frac{1}{4}\cos^2\beta\sin^2\chi$
$2\omega_r$	$\frac{1}{8}(-1+3\cos 2\beta)\sin^2\chi$
$2\omega_r+\omega_\oplus$	$\frac{1}{2}\cos\beta\sin\beta(\cos\chi+1)\sin\chi$
$2\omega_r+2\omega_\oplus$	$\frac{1}{8}\cos^2\beta(1+\cos\chi)^2$
$2\omega_r-\omega_\oplus$	$\frac{1}{2}\cos\beta\sin\beta(\cos\chi-1)\sin\chi$
$2\omega_r-2\omega_\oplus$	$\frac{1}{8}\cos^2\beta(1-\cos\chi)^2$

TABLE 2 Signal amplitudes (divided by Bv^2/c_0^2) for the experiment of Brillet and Hall

maximizes the sensitivity of the experiment to the anisotropy parameter of the RMS framework.

Within the SME, the cavity orientation is relatively unimportant: for the seven parameter combinations that can be determined by a MM experiment without a turntable, the cavity orientation in part determines the relative sensitivity of the experiments to the individual parameters, but there is no a priori reason why one should prefer a particular parameter.

3 Experimental aspects

Clearly, the challenges for performing relativity tests using cavities are to

(i) minimize any mechanical effects that change the cavity length, and
(ii) minimize any errors that occur in the read-out of the cavity frequency by means of the laser-frequency lock system.

In setting up our experiment, we have put substantial effort into satisfying these requirements.

3.1 *Cryogenic resonators and experimental apparatus*

Our CORE consist of a hollow 3-cm-long and 2.5-cm-diameter spacer and two mirrors fabricated from a single-crystal sapphire piece with the crystal c axis parallel

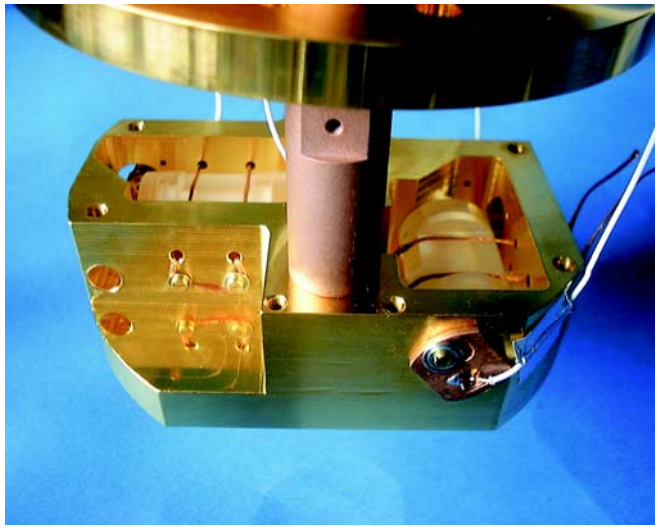

FIGURE 4 Cavity arrangement for the MM experiment. The two CORE are closely spaced and mounted inside a copper block to provide common-mode reduction of the influence of temperature variation: similar cavity-length changes do not affect the difference of the cavity frequencies

to the cavity axis (see Fig. 4). After polishing and coating the mirror substrates with a multilayer high-reflectivity dielectric stack, they were optically contacted to the spacer, maintaining the original crystal orientation. The optical line widths of the two CORE used are 50 kHz and 100 kHz, respectively; the finesses are of order 10^5.

The cryogenic operation of the sapphire resonators leads to a very low thermal expansion coefficient (10^{-10}/K at 4.2 K) and thus a low sensitivity to temperature changes. The creep of the cavities is not measurable at our current accuracy. Upper limits for the drift rates are < 2 kHz/6 months [12] and <0.1 Hz/h [23]. These characteristics represent a significant advantage over usual room-temperature resonators made from non-crystalline ultra-low-expansion glass ceramics (ULE or zerodur) that often exhibit drifts in the kHz/day range.

The CORE are operated inside a 4-K liquid-helium cryostat with optical access (see Fig. 5). The cryostat is equipped with a liquid-nitrogen shield. Liquid nitrogen is automati-

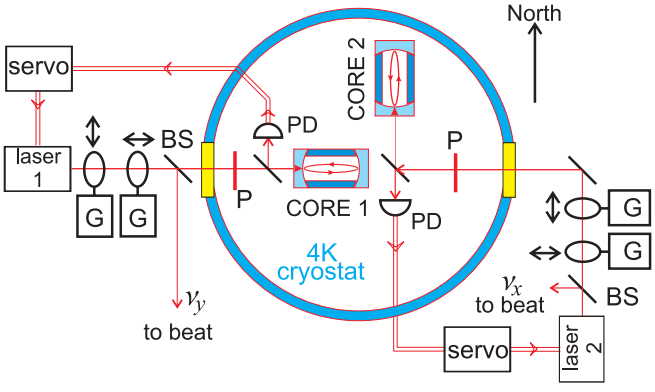

FIGURE 5 Setup of the Michelson–Morley experiment. Inside the cryostat two CORE are mounted orthogonally, with orientations north–south and east–west. Polarizers (P) and lock photodetectors (PD) are inside the cryostat. Galvo actuators (G) control laser-beam pointing (see Sect. 3.3). BS are beam splitters

cally refilled about every 3 h, while liquid helium is manually refilled approx. every 2 days. The lasers employed are monolithic, diode-pumped Nd : YAG lasers (Lightwave Electronics, Inc. and Innolight GmbH) emitting at 1064 nm with a very narrow line width (< 10 kHz). The beams are coupled into the resonators passing through the cryostat windows.

3.2 *Pound–Drever–Hall locking*

The requirement on the locking system is to provide the very best long-term stability. This differs from most other cavity frequency stabilization systems which are optimized to provide short-term stability (milliseconds to minutes).

For stabilizing a laser frequency ω_{L} to a resonance of a cavity at ω_{cav}, we use a modified Pound–Drever–Hall (PDH) locking system together with a method for offset compensation (Sect. 3.4). For PDH locking a phase modulation (PM) with a frequency ω_{m} and a modulation index β_{m} is applied to the laser beam. The beam is coupled to the cavity and the reflected signal is detected. The resonant and dispersive properties of the cavity near ω_{cav} convert the PM into amplitude modulation (AM) components at multiples of ω_{m}. At zero detuning, the detected component of the AM vanishes; otherwise a non-zero AM can be detected. The detected signal is multiplied with a local oscillator (LO) signal at ω_{m} with a phase ϕ relative to the PM signal in a double-balanced mixer (DBM), and the output of the DBM is low-pass filtered to suppress the modulation frequency ω_{m}. With the correct LO phase ϕ, a PDH error signal with a zero crossing at $\omega_{\mathrm{L}} = \omega_{\mathrm{cav}}$ is generated. This signal is fed back to the laser-frequency actuator via a suitable servo, which controls ('locks') ω_{L} such that $\omega_{\mathrm{L}} = \omega_{\mathrm{cav}}$.

Our implementation of the PDH technique differs from the usual approach in that we use $3\,\omega_{\mathrm{m}}$ instead of $1\,\omega_{\mathrm{m}}$ as the LO frequency. This gives an error signal as shown in Fig. 6. The maximum signal amplitude is then obtained for a PM modulation index $\beta = 3.95$. A PM index of $\beta = 3.83$ (where the first sidebands vanishes) is preferred for obtaining a signal without distortions from the first sideband, while losing only 1% of the signal amplitude. Compared to the usual $1\,\omega_{\mathrm{m}}$ technique, the $3\,\omega_{\mathrm{m}}$ method is relatively insensitive to residual AM produced by imperfections of the phase modulator. Theoretically, AM generates only first sidebands that do not contribute to the $3\,\omega_{\mathrm{m}}$ signal. Another advantage is that at the high modulation index used, most of the total laser power is contained in the sidebands. These do not enter the resonator if $\omega_{\mathrm{m}} \gg B$. Consequently, the $3\,\omega_{\mathrm{m}}$ method generates an about two times better error signal S/N ratio at the same laser power circulating inside the cavity. Furthermore, the higher detection frequency $3\,\omega_{\mathrm{m}}$ helps to overcome the technical noise floor of the Nd : YAG laser.

It is important to keep the power of the light circulating inside the cavity as low as possible to minimize the change of the resonance frequency due to laser heating of the cavities, $\sim 10\,\mathrm{Hz}/\mu\mathrm{W}$. At high laser powers, there seems to be a linear drift that is proportional to the laser power, but this was negligible for the low laser powers we employed. Using the $3\,\omega_{\mathrm{m}}$ technique and low-noise detection as described below, about 80 nW impinging on the COREs (not counting the laser power in the sidebands, that do not enter the CORE) was sufficient for locking with an error signal S/N ratio of $1.5 \times 10^4 \sqrt{\mathrm{Hz}}$. We reach a minimum instability of the locked laser frequency

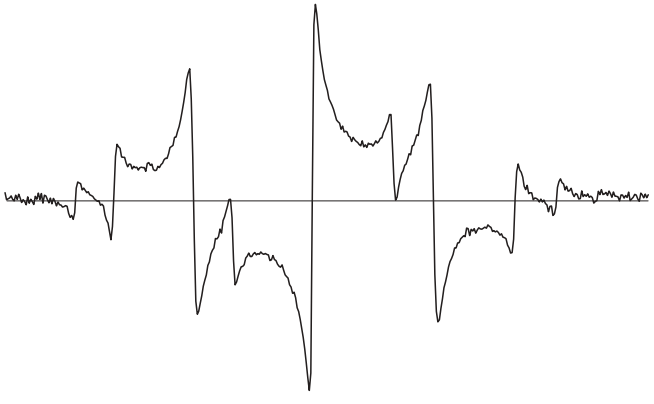

FIGURE 6 Measured Pound–Drever–Hall error signal generated by down conversion at $3\,\omega_m$ LO frequency. The modulation index β is 3.83, so that the first sideband vanishes. Otherwise, spikes would occur in the signal at $\omega_{\mathrm{L}} = \omega_{\mathrm{cav}} \pm 1\omega_{\mathrm{m}}$, between the central zero crossing and the zero crossing next to the center

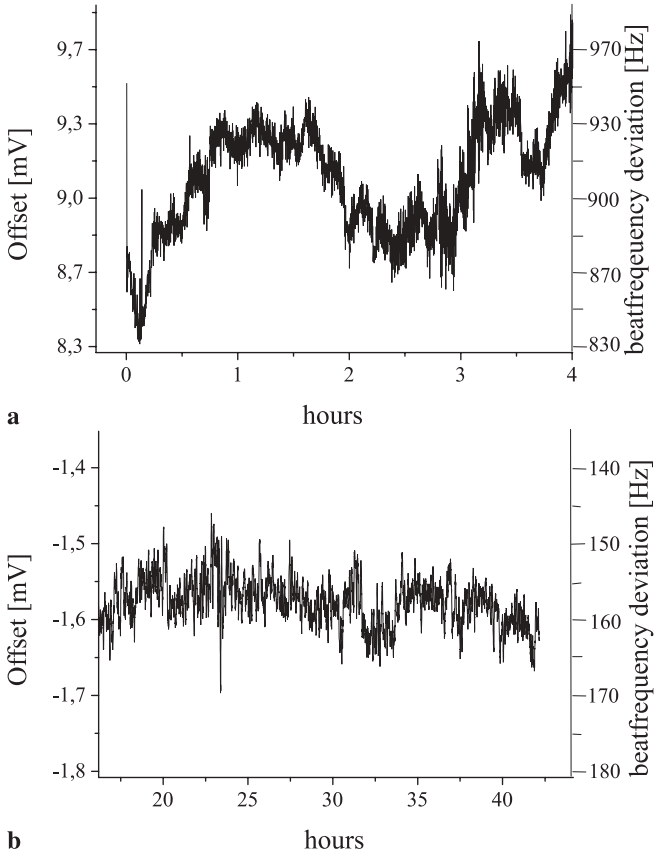

FIGURE 7 **a** Beat between two lasers locked using conventional PDH scheme. Shown is the lock error, the deviation of the lock point from the center of the cavity resonance, which was measured using the offset-compensation technique described in Sect. 3.4. The average lock error is about 900 Hz and varies by about 100 Hz peak to peak. **b** Same for two lasers locked using $3\,\omega_m$ PDH lock. The average error is about 150 Hz, with variations of about 10 Hz peak to peak, mostly due to noise

of 7×10^{-16} for integration times between 150 and 450 s [10]. Figure 7 shows two time traces from beat measurements between lasers locked using 1 ω_m and 3 ω_m locking. The advantages of the 3 ω_m method are clearly visible. Thus this method has been used for all but a few measurements at the very beginning of the experiment.

Using even harmonics 2 ω_m, 4 ω_m, ..., no dispersive signal with a zero crossing at $\omega_L = \omega_{cav}$ is generated. Instead, the 2 ω_m signal has a maximum at $\omega_L = \omega_{cav}$. While the laser is locked, this can be used for a stray light insensitive measurement of the fraction of laser power that is coupled to the cavity. This signal has been used for optimizing the coupling of the laser beams to the COREs by the automatic beam-positioning system (see Sect. 3.3).

3.2.1 Phase modulation of the laser beam. The standard method for modulating the phase of the laser beam is to employ an electro-optic modulator (EOM). By using an EOM, however, it is difficult to reliably obtain residual amplitude modulation (RAM) levels below 10^{-3} on a long time scale. Thus we employ the alternative method of Nd : YAG laser crystal strain modulation. Here the excitation frequencies are chosen to coincide with mechanical resonances of the laser crystal near 500 kHz[1].

3.2.2 Detection and amplification of the light reflected from the COREs. The lock detectors are mounted rigidly to the CORE holder inside the cryostat to avoid a relative movement of the detectors and the COREs that could strongly distort the PDH error signal. We use Epitaxx 2000 InGaAs detectors with a large active detector area of 2 mm^2, which makes the detector position (that might be slightly changed during cooling) uncritical. The detector output current is brought out of the cryostat via about 2-m long, 50-Ω miniature coaxial cables[2].

The large detector area leads to a high capacitance of the detectors of about 500 pF. Application of reverse bias of 5 V reduces this to 170 pF. The cable capacity of 100 pF/m has to be added to this, totaling about 500 pF. At 3 $\omega_m \sim 1.5$ MHz, this has a reactance of only about $|X_C| \sim 300\,\Omega$, making low current noise amplification of the detector signal extremely difficult. For reaching a current noise density i_n on the order of pA/Hz$^{1/2}$, the amplifier must not only have such a low current noise, but also a voltage noise less than $i_n|X_C| \sim 300$ pV/Hz$^{1/2}$. This corresponds to the noise generated by a 300-Ω resistor at a temperature of ~ 5.4 K.

As a first approach, we used a tank inductance to resonantly enhance X_C by a factor $Q \sim 20$. The tank coil itself must have an extremely high $Q \sim 200$, so that the tank circuit's Q factor is limited by the detector loss and cable resistances that are at cryostat temperature. Otherwise, the series resistance of the inductance at room temperature would generate appreciable additional noise. With a first amplifier stage using a dual-gate MOSFET (type BF981), an overall equivalent detector current noise of about 2 pA/Hz$^{1/2}$ was reached. However, this approach requires cumbersome retuning for every modulation-frequency change and is unable to amplify the signal components at 2 ω_m (for measuring the incoupling, see Sect. 3.3) and 3 ω_m (for locking) at the same time.

Thus we subsequently developed a broadband, paralleled MOSFET amplifier. The noise-voltage density at frequencies above the $1/f$ noise regime of a MOSFET can be roughly estimated by $u_n = (4k_B T r_n)^{1/2}$, where T is the operating temperature near room temperature and $r_n \simeq 0.65/s$ [24], where s is the transconductance of the FET. For low u_n, the transistors must therefore have high s, but at the same time low input capacitance C_1, in order not to reduce the input impedance further. MOSFET tetrodes BF1009 made for UHF receiver applications (by Infineon Technologies AG) were chosen. They have $C_1 = 2.1$ pF and $s \simeq 30$ mS at 14 mA, so $u_n \simeq 600$ pV/Hz$^{1/2}$ for a single transistor or $u_n \simeq 210$ pV/Hz$^{1/2}$ for eight devices in parallel is expected. A further increase of the number of paralleled transistors makes it difficult to keep the amplifier stable because of the high transconductance and UHF capabilities of the devices.

While the detector reactance is mainly capacitive (and therefore noise-free), additional noise is generated by the resistance R_c of the cable. At room temperature, $R_c \simeq 14\,\Omega$, generating 400 pV/Hz$^{1/2}$. Fortunately, most of the cable is at the cryostat temperature and does not generate an appreciable noise contribution. The detector series resistance, also at 4 K, does contribute to the total noise as well. Overall, we reach a measured noise performance (with the cryostat cooled down) of about 3 pA/Hz$^{1/2}$, corresponding to an optical noise of 3.8 pW/Hz$^{1/2}$. Slight improvements by approximately equal factors were achieved by applying a photodetector backward bias of 4.5 V to decrease the detector capacitance and by using an impedance-matching transformer in front of the amplifier input. A 1 : 1.5 voltage ratio with the high-impedance side at the amplifier input was found to give lowest noise. Ultimately, we measured about 2.7 pW/Hz$^{1/2}$ equivalent optical noise power density, comparable to the resonant amplifier. This level corresponds to the shot noise of a $\sim$ 50-μW beam. It allowed us to lock reliably at powers down to 80 nW impinging on the COREs.

3.2.3 Double-balanced-mixer operation. The selection and proper operation of the double-balanced mixer is crucial. On the one hand, it has to operate highly linearly to be able to suppress unwanted signal components [3]. This requires a signal amplitude well below saturation. On the other hand, the signal amplitude should be large compared to the mixer offset voltages. Thus, a compromise is needed that often involves rather high drive levels. We, however, operate the mixer in a way that emphasizes linearity. This produced results superior to the ones obtained by a strong rf drive.

[1] For the Lightwave electronics laser, at a modulation frequency of 226 kHz, a PM index of 1 was obtained at 2×10^{-5} RAM; the Innolight laser produced a PM index of 1 at RAM of 1.7×10^{-4} (at 150 kHz). The AM components at 3 ω_m were below a level of 10^{-5} in both cases.

[2] These transfer a significant amount of heat into the cryostat; only two of these reduce the standing time by 20%; however, they have superior electrical performance compared to special cryostat coaxial cables.

[3] This reduces the sensitivity of the stabilized laser frequency to parameters such as laser-power variations, beam alignment, polarization, or electromagnetic interference. These influences produce error-signal amplitude and phase changes, and also parasitic signals at other than the LO frequency. A non-linear DBM converts these to a DC signal that adds an offset to the error signal.

Type	Designation	$\Delta U/U_{max}$ (10–50°)
SAY-1 (a)	23 dBm mixer	133 ppm
SAY-1 (b)	23 dBm mixer	166 ppm
ZAD1-1	7 dBm mixer	700 ppm
ZAD-8 (a)	7 dBm mixer	< 25 ppm
ZAD-8 (b)	7 dBm mixer	50 ppm
ZRPD-1 (a)	Phase detector	3000 ppm [a]
ZRPD-1 (b)	Phase detector	20 000 ppm [a]

[a] This might be the result of improper handling prior to this measurement: exceeding the maximum ratings of the mixer can cause unbalance between the diodes inside the DBM, although it does not necessarily lead to complete failure

TABLE 3 Change of the dc IF voltage of some DBMs made by Mini-Circuits, Inc. for temperature changes between 20° and 50°. Both LO and rf were 500-kHz sine waves of 7-dBm and 23-dBm power respectively whose relative phase was adjusted such that the initial IF voltage was zero. Changing the temperature by about 30° using a heat gun produced the tabulated IF voltage changes that are expressed in ppm of the maximum output voltage obtained from that mixer with LO and rf in phase. The quick temperature change produced by a heat gun is quite unrealistic for laboratory conditions and was used as a worst-case scenario

Sample	U_{off} [mV]	$\delta\nu_L$ [Hz]
A	−20	50
B	−20	50
C	20	50
D	3	20

TABLE 4 Performance of four samples of SAY-1 mixers. Tabulated are the initial offset voltages U_{off} at 20 °C. The mixers were then installed in the MM system and the frequency change $\delta\nu_L$ due to mixer temperature changes under the conditions described in the caption of Table 3 was measured

To supply the mixer with as clean a signal as possible, elimination of electromagnetic interference[4] (quite easily detected using a spectrum analyzer) is essential. We band-pass filter the signal to remove wide-band noise and interference at remote frequencies. When using a $3\,\omega_m$ PDH scheme, such filtering is also required to suppress the $1\,\omega_m$ signal, which would otherwise generate unwanted $3\,\omega_m$ components due to non-linearities in the subsequent amplifier stages and the DBM itself. The peak rf amplitude at the mixer input (checked on an oscilloscope) is then adjusted to about 10–20 dB below the nominal rf amplitude for the mixer and amplifier types used.

We tested several mixer types made by Mini-Circuits, Inc. The results are given in Table 3. The lowest offset voltage and temperature sensitivity were found for ZAD-8-type mixers. However, the high LO level types SAY-1 were chosen because of the enhanced linearity they provide at a given signal level. Four samples of this type were checked within the complete CORE system (Table 4). Although the data does not warrant a definitive statement, a sample that has lower initial offset voltage does perform better in the PDH system. Analog multiplier chips might be a low-drift alternative to DBMs that are worthwhile testing, especially for lower LO frequencies.

[4] With the very low light levels we use, these are sometimes surprisingly strong, especially due to switching power supplies and horizontal deflection coils in instrumentation equipment of modern make (i.e. unshielded with plastic housing).

3.3 *Beam-alignment stabilization*

An automatic beam-alignment stabilization is used to compensate for the movements of the CORE s located inside the cryostats that are caused by refills and evaporation of coolants. These movements change the lock point, in part due to coupling to higher modes of the cavities and inhomogeneity of the lock detectors' active area, and possibly additional reasons.

For alignment stabilization, the laser beams pass through glass plates mounted under an angle of 45° relative to the beams, thus causing a parallel displacement of the beams. The angle can be controlled by ±6° using galvanometer drives, corresponding to a ±50-μm adjustment range of the beam displacement. For each beam, one glass plate controls the x and one the y displacement[5]. A displacement error signal is generated by dithering the tilt angles at frequencies in the range of 300–1000 Hz. The laser power coupled to the CORE s is measured and analyzed by lock-in amplifiers referenced to the tilt-angle modulation signal. This produces an incoupling error signal that is zero when the incoupling is optimum. Separate signals can be obtained for each galvanometer by using different modulation frequencies. The galvanometer tilt angle is then controlled by slow I servos[6].

As a stray light insensitive measure of the coupling efficiency, we use the $2\,\omega_m$ PDH error signal produced by the lock detectors in reflection. The amplitude of this signal is proportional to the laser power coupled into the cavity, while stray light that hits the detector without having entered the cavity before does not contribute.

3.4 *Offset compensation*

Using the PDH system, lock errors originate (i) from the generation and modulation of the oscillations (e.g. residual AM caused by the phase modulator), (ii) from the transmission of the oscillations to the reference (like parasitic resonances in the signal path), and (iii) from the generation of the error signal U_e (like temperature dependence of electronic circuits). For such reasons, a signal $U_e + U_o$ is generated instead of U_e. The lock point, where $U_e + U_o = 0$, is thus shifted to $\omega_{res} + \varepsilon_o$.

Since these influences can never be fully removed, a method is desirable to measure and compensate for these influences. We developed and successfully applied such a method (OCAMS = offset compensation by amplitude-modulated sidebands), which is the subject of a separate publication [25]. During several months of the measurement another previously developed method was implemented, which achieved a compensation of offsets on the error signal in a different way. Here an additional phase modulation with a constant amplitude was done at 10 MHz for the first (respectively 25 MHz for the second) laser using EOMs. Every 5 s

[5] Additional control of the beam direction could lead to further improvement, but was not implemented, as controlling the displacement only produced satisfactory results .

[6] For simultaneous operation of the offset compensation described in Sect. 3.4 and the beam-positioning systems, the time constant of the beam-stabilization servos was made large, so that they integrate over many frequency jumping and relocking cycles of the offset compensation, and the $2\omega_m$ signal detection was disabled for a period starting slightly before and ending slightly after the jump.

I	δI	$\delta_I \nu$[Hz]	$\delta_I^{\mathrm{OC}} \nu$ [Hz]
LO phase laser 1	10°	1200	< 10
LO phase laser 2	10°	80	< 10
β_{m} laser 1	+1%	50	–
β_{m} laser 2	+20%	–	−20
DBM temp.	30 °C	30...50	< 10
Laser power laser 1	4%	50	–
Laser power laser 2	30%	–	25

TABLE 5 CORE beat-frequency change due to variations δI of various influences (denoted I) without compensation of offset $\delta_I \nu$ and with compensation of offset $\delta_I^{\mathrm{OC}} \nu$

alternately the sideband of one of the lasers was automatically locked to the cavity instead of the carrier for 1 s. After that the carrier was automatically relocked again.

As the error signals produced by carrier and sidebands are of different amplitude, the offset on these signals, which is very nearly frequency independent, leads to different lock-point shifts when locking the carrier and the sidebands. From the measured beat frequencies during each locking interval, values for the lock-point shifts of both lasers $\varepsilon_{\mathrm{o},x,y}$ are calculated by a computer and correction signals can be added to the error signals via a D/A converter.

The correction signals were generated as the measured lock-point shifts $\varepsilon_{\mathrm{o},x,y}$ times factors A_x and A_y, plus the sum $\sum U_{\mathrm{corr},x,y}$ of all past correction voltages. This is to approximate an integral servo, which means that a constant offset is suppressed below any desired value after sufficient integration time. The constants were adjusted such that the time constant for suppressing an offset to about 1/2 of its original value was some 100 s.

The improvements in insensitivity of the beat frequency to external influences, which were achieved by applying active offset compensation, are summarized in Table 5.

4 Data analysis

Except for a 10-day break around New Year 2002, during which polarizers were installed in the cryostat, the CORE was operated continuously at 4.2 K over more than one year. Usable data (discounting data sets shorter than 12 h and data taken during adjustment or liquid-helium refills) started on June 19, 2001 and was acquired over 390 days until July 13, 2002.

4.1 *Cleaning and fitting the data*

In order to produce reliable and reproducible results an automated procedure for analyzing the data was developed. This was complicated by the fact that data of different quality had been obtained during the 390 days of measurement, e.g. because new techniques were tested. The crucial point here was to find objective criteria to distinguish perturbed data sets from data sets considered to be usable for an analysis, and to remove a few single outliers from a single data set.

For analyzing the data, it was first averaged into one-minute bins to reduce the amount of data points. Figure 8 shows a part of the raw data including several usable measurement periods that each show frequency fluctuations of some

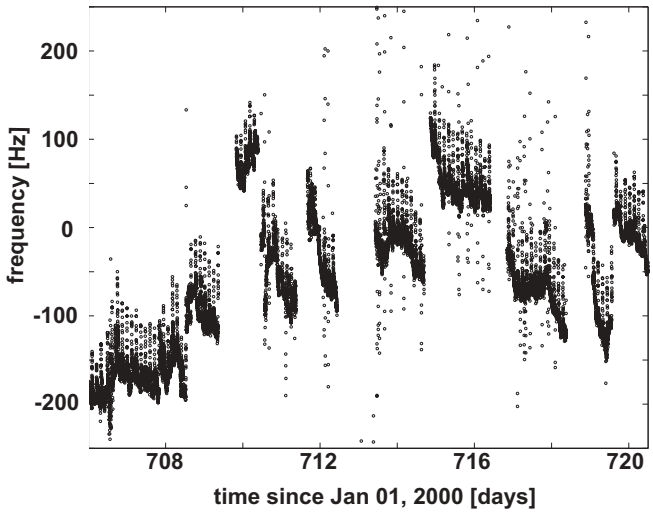

FIGURE 8 15 days of typical raw data. It shows several sections of usable data sets with typical lengths of 12 h to about two days, interrupted by off-lock periods. Sporadically, permanent offsets occur between the data sets, due to mechanical distortions of the setup probably caused by liquid-helium refills. Within the 15 days shown, peaks of about 50-Hz amplitude due to automatic liquid-nitrogen refills are visible every three hours. However, as they are of short duration, they do not significantly affect the fitting procedure

tens of Hz or less, separated by off-lock periods, e.g. due to helium refills and adjustments. Sometimes, especially in the first days after cooling down the cryostat, relaxation of mechanical strain built up during cooling causes permanent frequency shifts between the data sets. The off-lock periods were eliminated by hand and the data sets showing no such permanent shifts over at least 12 h were selected. This was the only manual action taken in the analysis. To remove large spikes (up to several MHz) still included in some of the remaining data (e.g. due to accidental interruption of the laser beam that enters the beat detector), all data points more than 100 kHz away from the average of a data set were removed. Thus, 146 pre-cleaned data sets of 12 h to 109 h in length were obtained.

To obtain limits on Lorentz violation in the frameworks provided by the SME or the RMS test theory, the pre-cleaned data is analyzed for a hypothetical sinusoidal isotropy violation signal at the frequencies suggested by the test theories.

For analysis at frequencies $2\omega_\oplus$, $2\omega_\oplus - \Omega_\oplus$, and $2\omega_\oplus + \Omega_\oplus$ only data sets > 12 h in length are considered. Similarly, for $\omega_\oplus$, $\omega_\oplus - \Omega_\oplus$, and $\omega_\oplus + \Omega_\oplus$ only data sets > 24 h are included. The pre-cleaned data sets are divided into subsets of 12 h (24 h). This removes a fraction of the data as remainders < 12 h (< 24 h) are discarded, but makes the fit results independent of offsets in the data. 199 non-overlapping, independent subsets of 12 h and 43 subsets of 24 h were used in total. In analyzing a subset we proceed as follows (Fig. 9): the average and standard deviation of the data subset are calculated. Points that deviate from the average by more than five standard deviations are discarded. Since at this stage the data usually contains a drift of 10–100 Hz/h and the standard deviation is correspondingly large, this is a very weak criterion. It removes large spikes that would lead to erroneous results in the final fitting procedure (see inset in Fig. 9). To remove possible remaining outliers, the subset is fitted with a constant

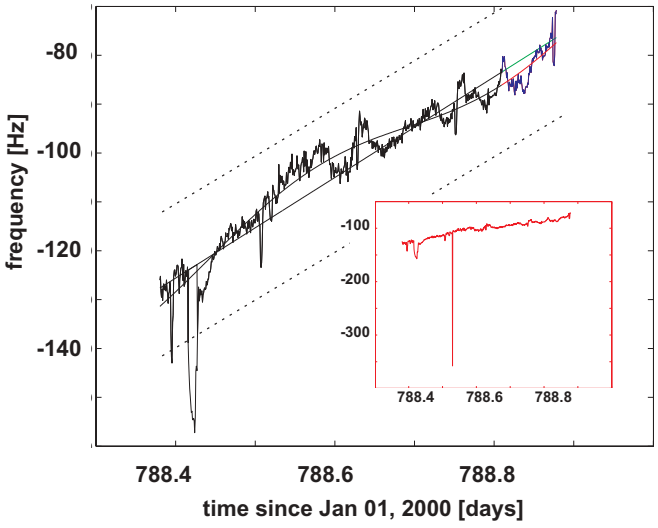

FIGURE 9 Removal of outliers and fit of violation signal in a 12-h data subset. Large spikes (see *inset*) are omitted by dropping all data points beyond $5\sqrt{\bar{\chi}^2}$ in a first step. Then a linear drift and offset are fitted to the data and all points more than $3\sqrt{\bar{\chi}^2}$ away from the fit (*dotted lines*) are considered outliers and are dropped. The remaining data points are least-squares fitted with a sinusoidal signal corresponding to RMS or SME with offset and linear drift as free parameters

offset and a linear drift, and the average square deviation $\bar{\chi}^2$ of the data from the fit is calculated. Data points that deviate from the fit by more than $3\sqrt{\bar{\chi}^2}$ are discarded. This cleaning removes only a minute amount of data ($< 1\%$).

The cleaned data subsets are least-squares fitted with the amplitude and phase of a sinusoidal signal at frequencies given by RMS or SME with offset and linear drift as free parameters. As a measure for the quality of a data set, the average $\bar{\chi}^2$ of the squared residuals for each fit was calculated. As a minimum requirement for the fit quality, we took $\sqrt{\bar{\chi}^2} < 20$ Hz. This criterion was violated for 25 subsets of 12 h and one subset of 24 h. In these cases, the first 1–3 h of the pre-cleaned data set (that likely contained perturbations from a preceding helium refill) were discarded, and the cleaning and fitting procedure was repeated with the subsequent 12 h. This allowed us to re-introduce eight of the 25 perturbed 12-h subsets into the analysis.

The average and standard error calculated from the distribution of the individual fit results were taken as the final result[7]. Coherent (vector) averaging was used, i.e. the fitted amplitude and phase of the individual data sets were projected onto the sine and cosine components of the hypothetical signal prior to averaging.

The above cleaning and fitting procedure has been carried through completely automated by a computer program. To check the reliability of the method and the program, test data sets were constructed by superimposing an artificial signal of known amplitude (between 10 Hz and 50 Hz) and phase on the complete 390 days of actual data, with all interruptions, outliers, etc. The test data sets were then run through the above procedure, and the results obtained were compared to

[7] The formal error bars for the fit results are not suitable as the error of the final result, as for their determination one assumes that the data points within a data set are each individual, uncorrelated measurements.

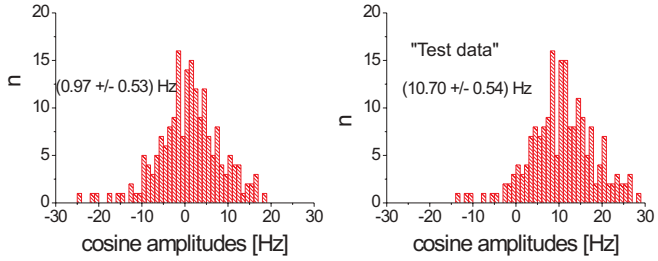

FIGURE 10 *Left*: Histogram of SME-fit results at $\cos 2\omega_\oplus t$ from the original data. *Right*: Histogram of fit results at $\cos 2\omega_\oplus t$ from the original data plus a sinusoidal test data set of 10 Hz $\cdot\cos 2\omega_\oplus t$

the known amplitude of the artificial signal. It was found that the fit results obtained were equal to the artificial signal amplitude within an error that was consistent with the error bar of the results (see Fig. 10).

4.2 *Final result in the RMS framework*

For the analysis within the RMS formalism, the hypothetical signal consists of components at $\omega_\oplus$ and $2\omega_\oplus$ (35). The fit results for these frequencies in principle allow us to deduce two independent limits on the RMS anisotropy parameter B; however, the limit from the $\omega_\oplus$ fit result is weaker. For the $2\omega_\oplus$ component, we obtain a signal of 1.03 ± 0.53 Hz, or $\Delta c/c = (3.7 \pm 1.9) \times 10^{-15}$. As the data quality is not uniform, (Fig. 11), taking a weighted average is more appropriate. We divide the data into the groups A–E with approximately uniform data quality within each. The average and standard error of each interval are then calculated (Table 6). These results are then combined for the final result weighted according to their standard error. Thus, we obtain a signal amplitude of 0.73 ± 0.48 Hz, or $\Delta c/c = (2.6 \pm 1.7) \times 10^{-15}$.

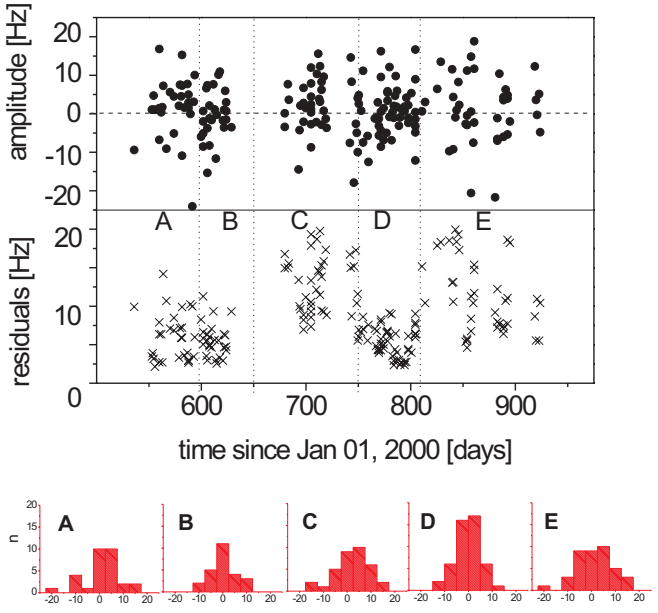

FIGURE 11 Distribution of RMS-fit results over time for signals at $\cos 2\omega_\oplus t$ and distribution of fit residuals. The data is grouped into five sections of different quality. The histograms for each single group are shown *below*, the mean values and standard errors of which are given in Table 6

Group	N	A_C [Hz]	A_S [Hz]
A	33	1.05 ± 1.41	-2.66 ± 1.31
B	28	0.26 ± 1.12	1.25 ± -0.84
C	40	2.2 ± 1.23	-0.14 ± 1.39
D	55	-0.09 ± 0.76	-0.43 ± 0.56
E	43	1.68 ± 1.21	-0.77 ± 1.39
weighted average	199	0.72 ± 0.48	-0.26 ± 0.40

TABLE 6 Amplitudes of the $2\omega_\oplus$ modulation within the RMS analysis. N denotes the number of subsets contained in each group. A_C and A_S denote the cosine and sine amplitudes respectively

ω_i	A_i^S [Hz]	A_i^C [Hz]
$\omega_\oplus - \Omega_\oplus$	$\mathbf{1.82 \pm 1.91}$	0.67 ± 1.58
$\omega_\oplus$	$\mathbf{-0.51 \pm 1.26}$	$\mathbf{0.89 \pm 1.74}$
$\omega_\oplus + \Omega_\oplus$	-0.43 ± 1.68	1.83 ± 1.83
$2\omega_\oplus - \Omega_\oplus$	$\mathbf{-0.01 \pm 0.57}$	$\mathbf{0.25 \pm 0.55}$
$2\omega_\oplus$	$\mathbf{0.37 \pm 0.56}$	$\mathbf{0.97 \pm 0.53}$
$2\omega_\oplus + \Omega_\oplus$	0.50 ± 0.55	-0.75 ± 0.58

TABLE 7 Results for the signal amplitudes from the SME. The total signal (23) can be written as $(v_x - v_y)/\bar{v} = \sum_i A_i^S \sin \omega_i T_\oplus + A_i^C \cos \omega_i T_\oplus$, where the signal amplitudes of (23) are denoted A_i^S and A_i^C ($i = 1, ..., 6$). $\omega_\oplus \approx 2\pi/(23\,\mathrm{h}\,56\,\mathrm{min})$ and $\Omega_\oplus = 2\pi/1\,\mathrm{yr}$ denote the angular frequencies of Earth's sidereal rotation and orbit. A fit result that has been used to extract a parameter of the SME is set in *bold face*. The unused fit results lead to additional (but weaker) limits on the elements of $\tilde{\kappa}_{o+}$

Following the analysis in Sect. 2.2 this leads to

$$B = (-2.2 \pm 1.5) \times 10^{-9}, \tag{38}$$

which we regard as our final result. The result of the experiment by Brillet and Hall [8] led to a signal amplitude $\delta\nu/\nu = (1.5 \pm 2.5) \times 10^{-15}$ at a signal frequency of $2\omega_r + 2\omega_\oplus$. Comparing with the hypothetical signal amplitude given in Table 7 for that frequency gives $B = (3.0 \pm 4.9) \times 10^{-9}$. Wolf et al. [11] reported a comparable limit of $B = (1.5 \pm 4.2) \times 10^{-9}$.

4.3 *Standard model extension results*

For analysis within the SME, the hypothetical signal is given by (23). It consists of sine and cosine components at six different frequencies. Because of the > 1-yr duration of our data, in the vector average we can resolve the six frequencies. This allows us to extract separate limits on all seven different Lorentz-violation parameters contained in the hypothetical signal. Weighted averages have not been taken, as this would have increased the interdependency of the results for the six frequencies. The fit results are given in Table 2. These give a limit on the traceless symmetric matrix

$$\tilde{\kappa}_{e-} = \begin{pmatrix} a & 1.7 \pm 2.6 & -6.3 \pm 12.4 \\ 1.7 \pm 2.6 & b & 3.6 \pm 9.0 \\ -6.3 \pm 12.4 & 3.6 \pm 9.0 & -(a+b) \end{pmatrix} \times 10^{-15},$$

with $a - b = 8.9 \pm 4.9$ (in the Sun-centered celestial equatorial reference frame of [6]). Likewise,

$$\tilde{\kappa}_{o+} = \begin{pmatrix} 0 & 14 \pm 14 & -1.2 \pm 2.6 \\ -14 \pm 14 & 0 & 0.1 \pm 2.7 \\ 1.2 \pm 2.6 & -0.1 \pm 2.7 & 0 \end{pmatrix} \times 10^{-11}$$

for the antisymmetric matrix, which enters the experiment suppressed by $\beta_\oplus$. Thus, all elements of $\tilde{\kappa}_{o+}$ and all but one element of $\tilde{\kappa}_{e-}$ are obtained. Our results can be compared to the ones by Lipa et al. [9]. Their values are generally of order 10^{-13} for $\tilde{\kappa}_{e-}$ and of order 10^{-9} for $\tilde{\kappa}_{o+}$; thus, our measurement has an accuracy about two orders of magnitude higher. Furthermore, while [9] gives linear combinations of the components of $\tilde{\kappa}_{o+}$, our experiment allows individual determination. This is because the >1-yr span of our data allows us to separate results for all six signal frequencies.

5 Summary and outlook

In conclusion, we have performed a modern Michelson–Morley experiment that compared the frequencies of two crossed cryogenic optical resonators subject to Earth's rotation over more than one year. The limit we obtained on the isotropy-violation parameter within the Robertson–Mansouri–Sexl framework is about three times lower than that from the experiment of Brillet and Hall [8]. Furthermore, we obtained limits on seven parameters from the photonic sector of the standard model extension [6], at accuracies down to 10^{-15}, which is about two orders of magnitude lower than the only previous result [9].

For a future setup of the experiment active rotation on a turntable could improve the accuracy significantly. The low drift of CORE s compared to ULE cavities allows a relatively slow rotation rate, which is desirable for minimizing the systematic errors connected to active rotation. At a rate of ~ 0.2/min the optimum $\sim 7 \times 10^{-16}$ frequency stability of the CORE s at integration times of $\tau = 100$ s could be utilized, which is more than 10 times better than on the 12-h time scale used so far. Accumulating ~ 500 measurements per day (two per turn), one should thus be able to reach the 10^{-17} level of accuracy. Further improvements include fiber coupling and CORE s of higher finesse. New state of the art CORE s should be able to offer a 10-fold decrease in line width, which should directly lead to a corresponding improvement in lock stability. Altogether a 100–1000-fold improvement in accuracy should be within reach in the near future.

ACKNOWLEDGEMENTS We thank Claus Lämmerzahl for many valuable discussions and Jürgen Mlynek for making this project possible. This work has been supported by the Deutsche Forschungsgemeinschaft and the Optik-Zentrum Konstanz.

REFERENCES

1 A.A. Michelson: Am. J. Sci. **22**, 120 (1881); A.A. Michelson, E.W. Morley: Am. J. Sci. **34**, 333 (1887)
2 V.A. Kostelecký, S. Samuel: Phys. Rev. D **39**, 683 (1989)
3 R. Gambini, J. Pullin: Phys. Rev. D **59**, 124 021 (1999)
4 J. Alfaro, H.A. Morales-Técotl, L.F. Urrutia: Phys. Rev. Lett. **84**, 2318 (2000)
5 V.A. Kostelecky, M. Mewes: Phys. Rev. Lett. **87**, 251 304 (2001)
6 V.A. Kostelecky, M. Mewes: Phys. Rev. D **66**, 056 005 (2002)
7 D. Colladay, V.A. Kostelecký: Phys. Rev. D **55**, 6760 (1997); **58**, 116 002 (1998); R. Bluhm, V.A. Kostelecký, C.D. Lane, N. Russell: Phys. Rev. Lett. **88**, 090 801 (2002) and references therein
8 A. Brillet, J.L. Hall: Phys. Rev. Lett. **42**, 549 (1979)
9 J.A. Lipa, J.A. Nissen, S. Wang, D.A. Stricker, D. Avaloff: Phys. Rev. Lett. **90**, 060 403 (2003)

10 H. Müller, S. Herrmann, C. Braxmaier, S. Schiller, A. Peters: Phys. Rev. Lett. **91**, 020401 (2003)
11 P. Wolf, S. Bize, A. Clairon, A.N. Luiten, G. Santarelli, M.E. Tobar: Phys. Rev. Lett. **90**, 060402 (2003)
12 C. Braxmaier, H. Müller, O. Pradl, J. Mlynek, A. Peters, S. Schiller: Phys. Rev. Lett. **88**, 010401 (2001)
13 H. Müller, C. Braxmeier, S. Herrmann, O. Pradl, C. Lämmerzahl, J. Mlynek, S. Schiller, A. Peters: Int. J. Mod. Phys. D **11**, 1101 (2002)
14 S. Buchman, M. Dong, W. Moeur, S. Wang, J.A. Lipa, J.P. Turneaure: Adv. Space Res. **25**, 1251 (2000)
15 C. Lämmerzahl, H.-J. Dittus, A. Peters, S. Schiller: Class. Quantum Grav. **18**, 2499 (2001)
16 S.M. Carroll, G.B. Field, R. Jackiw: Phys. Rev. D **41**, 1231 (1990)
17 H. Müller, C. Braxmeier, S. Herrmann, A. Peters, C. Lämmerzahl: Phys. Rev. D **67**, 056006 (2003)
18 H.P. Robertson: Rev. Mod. Phys. **21**, 378 (1949); R.M. Mansouri, R.U. Sexl: Gen. Relat. Grav. **8**, 497 (1977); **8**, 515 (1977); **8**, 809 (1977)
19 C. Lämmerzahl, C. Braxmeier, H.-J. Dittus, H. Müller, A. Peters, S. Schiller: Int. J. Mod. Phys. D **11**, 1109 (2002)
20 R. Grieser, R. Klein, G. Huber, S. Dickopf, I. Klaft, P. Knobloch, P. Merz, F. Albrecht, M. Grieser, D. Habs, D. Schwalm, T. Kühl: Appl. Phys. B **59**, 127 (1994)
21 In early 2003 the group announced a four-fold improvement of the experiment (G. Gwinner, G. Saathoff, S. Karpuk, U. Eisenbarth, G. Huber, S. Krohn, R. Munoz-Horta, S. Reinhardt, D. Schwalm, M. Weidemüller, A. Wolf: in *DPG Spring Meet., Hannover 2003*)
22 C.H. Lineweaver, L. Tenorio, G.F. Smoot, P. Keegstra, A.J. Banday, P. Lubin: Astrophys. J. **470**, 38 (1996)
23 S. Seel, R. Storz, G. Ruoso, J. Mlynek, S. Schiller: Phys. Rev. Lett. **78**, 4741 (1997); R. Storz, C. Braxmeier, K. Jäck, O. Pradl, S. Schiller: Opt. Lett. **23**, 1031 (1998)
24 R.S.C. Cobbold: *Theory and Applications of Field-effect Transistors* (Wiley, New York 1970) p. 319
25 H. Müller, S. Herrmann, T. Schuldt, M. Scholz, E. Kovalchuck, A. Peters: to appear in Opt. Lett., issue date 11/15/03 (2003)